Phys. Med. Biol. **43** (1998) 905–920. Printed in the UK PII: S0031-9155(98)89759-5

Quantitative cardiac SPECT in three dimensions: validation by experimental phantom studies

Z Liang†, J Ye, J Cheng, J Li and D Harrington

Departments of Radiology, Computer Science and Electrical Engineering, State University of New York, Stony Brook, NY 11794, USA

Received 10 July 1997

Abstract. A mathematical framework for quantitative SPECT (single photon emission computed tomography) reconstruction of the heart is presented. An efficient simultaneous compensation approach to the reconstruction task is described. The implementation of the approach on a digital computer is delineated. The approach was validated by experimental data acquired from chest phantoms. The phantoms consisted of a cylindrical elliptical tank of Plexiglass, a cardiac insert made of Plexiglass, a spine insert of packed bone meal and lung inserts made of styrofoam beads alone. Water bags were added to simulate different body characteristics. Comparison between the quantitative reconstruction and the conventional FBP (filtered backprojection) method was performed. The FBP reconstruction had a poor quantitative accuracy and varied for different body configurations. Significant improvement in reconstruction accuracy by the quantitative approach was demonstrated with a moderate computing time on a currently available desktop computer. Furthermore, the quantitative reconstruction was robust for different body characteristics. Therefore, the quantitative approach has the potential for clinical use.

1. Introduction

SPECT (single photon emission computed tomography) has been shown to provide useful information on the metabolic and physiologic functions of organs through the reconstructed images of radiopharmaceutical uptake distributions (Alavi 1977, Berman *et al* 1991, Maurea *et al* 1995, Nakajima *et al* 1993). Currently available SPECT protocols support only qualitative uptake images (Bartlett *et al* 1995, DePuey and Garcia 1989, Eisner *et al* 1994, Galt *et al* 1990, Garcia *et al* 1990). Although the diagnosis based on the qualitative images has succeeded in many cases, the sensitivity and specificity have not yet met our expectations, especially for diagnosis of heart disease (Bartlett *et al* 1995, DePuey and Garcia 1989, Garcia *et al* 1990), where the thoracic heterogeneity and the cardiac and respiratory motion render a very challenging and currently unsolved problem.

It is well understood that quantitative SPECT will improve sensitivity and specificity of patient diagnosis (Bailey *et al* 1987, Hasegawa *et al* 1990, Jaszczak *et al* 1984, Links *et al* 1990, Tsui *et al* 1989, VanTrain *et al* 1980). A quantitative reconstruction of the uptake image of radiotracer distribution requires a simultaneous compensation for (1) attenuation of primary photons inside the body, (2) inclusion of scattered photons from the body in the measured data of photopeak-energy window and (3) variable detector resolution at

† Correspondence to: Z Liang, PhD, Department of Radiology, 4th Floor, Room 092/HSC, State University of New York at Stony Brook, Stony Brook, NY 11794-8460, USA. E-mail address: jzl@clio.rad.sunysb.edu

0031-9155/98/040905+16$19.50

different depths from the detector, as well as suppression of noise propagation in the image reconstruction, in addition to correction of patient motion, detection dead time and isotope decay (Floyd *et al* 1986, Gullberg 1979, Liang *et al* 1989, Zeng and Gullberg 1991).

Many quantitative approaches have been proposed in the past decades (Chang 1978, Furuie and Mascarenhas 1992, Glick *et al* 1994, 1995, Gullberg 1979, Jaszczak *et al* 1984, King *et al* 1983, 1992, Lewitt *et al* 1989, Liang *et al* 1989, Moore *et al* 1989, Ogawa *et al* 1991, Tsui *et al* 1989, Ye and Liang 1994b, Zeng and Gullberg 1991). Some of them addressed the degrading effects individually and others addressed the effects simultaneously. The major obstacle in implementing those simultaneous compensation approaches is the extremely heavy computing burden (Bouman and Sauer 1996, Clinthorne *et al* 1993, Fessler 1995, Hudson and Larkin 1994, Wallis and Miller 1993, Xu *et al* 1993). This work validated an efficient simultaneous compensation approach for quantitative SPECT reconstruction of the heart.

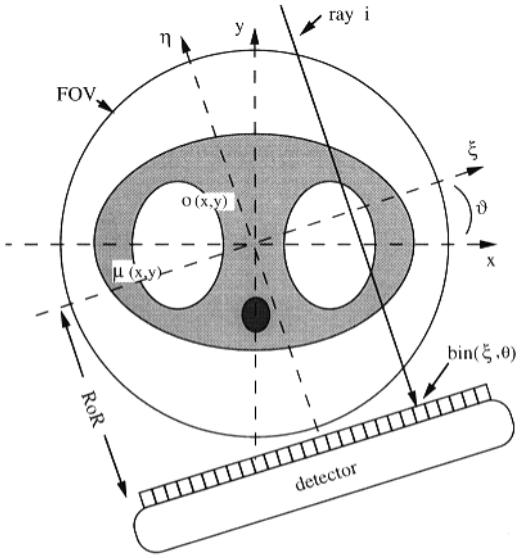

Figure 1. Two-dimensional representation of image reconstruction from projections for cardiac SPECT. The x–y is the source stationary coordinates and ξ–η is the detector rotation coordinates. The activity $o(x, y)$ may distribute across the chest inside the soft tissues (including the heart) and the lungs. The attenuation $\mu(x, y)$ is nonuniform due to mainly the lungs and secondarily the bone. The field of view (FOV) is defined by the size of collimator surface. In ideal collimation, all rays are parallel to the η axis.

2. Theory

This section presents a mathematical framework for quantitative SPECT reconstruction in object-specific attenuating media. The measured photon counts by a SPECT system from the photopeak-energy window at projection angle θ is expressed, see figure 1, as

$$m_p(\xi, z, \theta) = \tilde{p}_p(\xi, z, \theta) + n_p(\xi, z, \theta) \tag{1}$$

where m_p is the measured number of photons at detector bin (ξ, z, θ) (the ξ–z plane is the detection plane and the z axis is the detector-rotation axis); $\tilde{p}_p$ is the projection at angle θ of

radiotracer distribution or source $o(x, y, z)$ and n_p is the Poisson noise which is associated with the measurement m_p and depends on the signal $\tilde{p}_p$. The projection data $\tilde{p}_p$ include both the primary-photon contribution p_p and the scattered ones' p_s

$$\tilde{p}_p(\xi, z, \theta) = p_p(\xi, z, \theta) + p_s(\xi, z, \theta). \tag{2}$$

The projected number of primary photons p_p in the photopeak-energy window is given by

$$p_p(\xi, z, \theta) = \int_{-\infty}^{\infty} \mathrm{d}\eta \iint_{-\infty}^{\infty} \mathrm{d}\xi' \, \mathrm{d}z' \, h(\xi - \xi', z - z', \eta) A(\xi, \xi', \eta, z, z', \theta, e_p) o(\xi', \eta, z', \theta) \tag{3}$$

where $o(\xi, \eta, z, \theta)$ represents the source $o(x, y, z)$ in the rotated (detector) coordinates ξ–η–z at rotation angle θ. $A(\xi, \xi', \eta, z, z', \theta, e_p) = \exp[-\int_{-\infty}^{\eta} \mu(\xi', \eta', z', \theta, e_p) \, \mathrm{d}l]$ is the attenuation factor along line l from bin (ξ, z, θ) to point (x', y', z'), see figure 2, and $\mu(\xi, \eta, z, \theta, e_p)$ stands for the attenuation-coefficient distribution $\mu(x, y, z, e_p)$ in the rotated coordinates for primary-photon energy e_p. When the radiotracer $o(x, y, z)$ distributes inside nonuniform attenuating media, for example in chest imaging, an object-specific attenuation map $\mu(x, y, z, e_p)$ is necessary, which is obtained conventionally by transmission scans of the object (Bailey *et al* 1987, Hasegawa *et al* 1990, Liang and Ye 1994). Function $h(\xi, z, \eta)$ is the detector-response kernel characterizing the depth-dependent detector-resolution variation (see figure 2), which can be constructed from measurements of a point source in air at different depths RoR $+ \eta$, (RoR is the radius of rotation), from the collimator surface. For a flat collimator surface, the resolution kernel $h(\xi, z, \eta)$ is usually assumed as spatially invariant at a constant depth RoR $+ \eta$, i.e., $h(\xi, z, \eta)$ is spatially invariant in the ξ–z plane for a constant η (Liang *et al* 1989, Tsui and Gullberg 1990, Ye and Liang 1994a, Zeng and Gullberg 1991).

The included number of scattered photons p_s in the photopeak-energy window can be written as

$$\begin{aligned} p_s(\xi, z, \theta) = & \int_{-\infty}^{\infty} \mathrm{d}\eta \iint_{-\infty}^{\infty} \mathrm{d}\xi' \, \mathrm{d}z' \, h(\xi - \xi', z - z', \eta) A(\xi, \xi', \eta, z, z', \theta, e_s) \\ & \times \iiint_{-\infty}^{\infty} \mathrm{d}\xi'' \, \mathrm{d}\eta'' \, \mathrm{d}z'' \, S(\xi, \eta, z, \theta, \xi', z', \xi'', \eta'', z'') o(\xi'', \eta'', z'', \theta) \end{aligned} \tag{4}$$

where $S(\xi, \eta, z, \theta, \xi', z', \xi'', \eta'', z'')$ is the surviving probability that a photon is emitted from point (x'', y'', z''), passed through to point (x', y', z') (after attenuation at the primary-photon energy e_p), and then scattered into detector bin (ξ, z, θ) after attenuation $A(\xi, \xi', \eta, z, z', \theta, e_s)$ at scatter-photon energy e_s which is within the photopeak-energy window, see figure 2. The integral $\int\int\int_{-\infty}^{\infty} S(.) o(.) \, \mathrm{d}\xi'' \, \mathrm{d}\eta'' \, \mathrm{d}z''$ over the field of view (FOV) gives the scattered photons at point (x', y', z') contributing to bin (ξ, z, θ). Their contribution is affected, as for the primary photons, by both the attenuation and the depth-dependent resolution variation, see (3). The scatter factor $S(.)$ can be computed theoretically, given the attenuation map $\mu(x, y, z, e_p)$, by the use of the Klein–Nishina formula.

Given the noise property of photon measurements by (1) and (2) and the physics model of photon propagation in attenuating media by (3) and (4), a unified statistical algorithm could be employed to reconstruct accurately the radiotracer uptake image, based on a Bayesian inference (for example, see the work of Fessler (1995) and Liang and Hart (1988) among many others). The noise statistics can be modelled by a Poisson likelihood function and the noise propagation from data to image can be suppressed by including, in terms of probability, valid *a priori* source information. The image is then determined by optimizing

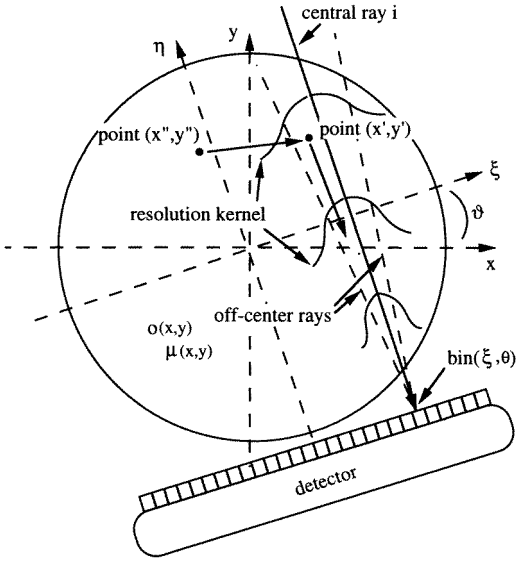

Figure 2. Two-dimensional description of detector-resolution variation and photon scatter. The rays parallel to the η-axis at a projection angle θ are called central rays. Others are called off-centre rays which are within the view angle subtended by the collimator holes. The contributions along the central and off-centre rays are weighted by the resolution kernel depending on the depths from the collimator surface. The scatter contribution is defined as those photons which are emitted outside the view of collimator holes, e.g., point (x'', y''), scattered into bins, e.g., bin (ξ, θ), and accepted within the photopeak window.

the *a posteriori* probability. The attenuation, scatter, and resolution variation are considered in the projection formulation via (2)–(4)

$$\tilde{p}_p(\xi, z, \theta) = \int\int\int_{-\infty}^{\infty} \mathrm{d}\eta \, \mathrm{d}\xi' \, \mathrm{d}z' \, R(\xi, \xi', \eta, z, z', \theta) o(\xi', \eta, z', \theta) \tag{5}$$

where $R(\xi, \xi', \eta, z, z', \theta)$ is the projection matrix which projects the source $o(x, y, z)$ to the noise-free data or means $\tilde{p}_p(\xi, z, \theta)$ at angle θ. Although this unified reconstruction is mathematically exact, the computation burden for (5) is prohibitively heavy (since $R(.)$ depends on the attenuation factor, the scatter contribution and the detector-resolution kernel), even if a supercomputer and a fast-convergent numerical technique are employed (Bouman and Sauer 1996, Clinthorne *et al* 1993, Hudson and Larkin 1994, Wallis and Miller 1993, Xu *et al* 1993). Alternative efficient approaches are clinically demanded. In the following section, an efficient approach based on (1)–(4) is described, which treats the Poisson noise, the photon attenuation and scatter and the detector-resolution variation in a coherent manner.

3. Method

The efficient compensation approach to the quantitative reconstruction of source distribution follows the steps below.

(1) *Treatment of Poisson noise.* This step is performed first in order to minimize noise propagation in the compensation of attenuation, scatter and resolution variation. The goal of this step is to estimate the signal $\tilde{p}_p$ from the measurement m_p, as shown by (1). A promising statistical approach to the goal is Wiener filtering which is based on the stochastic process

of measurement (Furuie and Mascarenhas 1992). Since the measured counts m_p is Poisson variate with variance equal to its mean $\tilde{p}_p$ (i.e., it is signal dependent), approximations are needed to design a Wiener filter for m_p (King *et al* 1983, Links *et al* 1990). To avoid the approximations, we convert the variable m_p into a signal-independent Gaussian variate by applying the square-root transformation (Anscombe 1948). This conversion offers another very attractive feature that the variance becomes a known constant of 0.25. In the square-root space, a Wiener filter can be accurately constructed (Cheng *et al* 1996); therefore, a better estimate of $\tilde{p}_p$ is expected from measured data m_p, as compared to the approximated Wiener approach which deals with the Poisson data directly.

(2) *Estimation of scatter contribution.* If the scatter contribution p_s to the projection $\tilde{p}_p$ of photopeak-energy window can be estimated, a subtraction by (2) for p_p would be the most efficient technique for scatter compensation. We adapt the dual-energy-window acquisition protocol (Jaszczak *et al* 1984) to estimate the scatter contribution p_s by

$$m_s(\xi, z, \theta) = \tilde{p}_s(\xi, z, \theta) + n_s(\xi, z, \theta) \tag{6}$$

where m_s is the measurement at bin (ξ, z, θ) from the off-photopeak or scatter-energy window and n_s is the Poisson noise associated with its signal $\tilde{p}_s$. By applying the noise reduction technique of step one to m_s for an estimate of $\tilde{p}_s$, then determining p_s and finally through (2) for scatter subtraction, we obtain the primary-photon contribution p_p to the photopeak-energy window, see (3).

In order to adequately estimate the scatter contribution p_s to the photopeak projection, the noise-reduced scatter-window data $\tilde{p}_s$ are smoothed by a low-pass Hann window at 0.25 Nyquist frequency cutoff (Huesman *et al* 1977) before employing the spectral analysis (Ogawa *et al* 1991)

$$p_s(\xi, z, \theta) = \frac{w_p}{2w_s}\tilde{p}_s(\xi, z, \theta) \tag{7}$$

where w_p and w_s are the width of the photopeak and off-peak energy windows, respectively. When $w_p = w_s$, this estimation reduces to a modified version of the approach of Jaszczak *et al* (1984). A relatively wide w_s has better statistical information as compared to a narrow w_s as described by Ogawa *et al* (1991). After scatter subtraction, the quantitative reconstruction becomes to invert (3) for $o(x, y, z)$.

(3) *Restoration of detector resolution.* Equation (3) could be a convolution of $h(\xi, z, \eta)^* o(\xi, \eta, z, \theta)$ for a constant depth RoR$+\eta$ at projection angle θ, if attenuation is not present. This is because of the spatial invariance of kernel $h(.)$ at a constant depth and the independence of source $o(.)$ from the location of detector bins. However, when attenuation is present, the depth-dependent convolution no longer exists due to the attenuation factor $A(\xi, \xi', \eta, z, z', \theta)$ (where e_p is omitted for convenience), which depends on coordinates of source point (ξ', η, z') and detector bin (ξ, z, θ). This dependence has an extremely high computing price (Liang *et al* 1989). An approximation can be very helpful.

In order to obtain the depth-dependent convolution, we approximate the attenuation factors along the off-centre rays (along line l) by that of the central ray (parallel to η axis for parallel-beam geometry), see figure 2. For a source slice $o(\xi, \eta, z, \theta)$ parallel to the collimator surface with a distance of RoR $+ \eta$, we compute the attenuation factors $A(\xi, \eta, z, \theta)$ along the central rays for all bins (ξ, z, θ) and then multiply, respectively, the factors by that source slice. The attenuated source slice $[A(.)o(.)]$ now does not depend on the coordinates of the bins at projection angle θ. A depth-dependent convolution, therefore, holds for the attenuated source slice and the kernel. Summation over all the attenuated source slices (parallel to the collimator surface) along the central rays gives the projection

data at that projection angle θ. Mathematically, (3) is approximated as

$$p_p(\xi, z, \theta) \approx \int_{-\infty}^{\infty} \mathrm{d}\eta \iint_{-\infty}^{\infty} \mathrm{d}\xi' \, \mathrm{d}z' \, h(\xi - \xi', z - z', \eta)[o(\xi', \eta, z', \theta)A(\xi', \eta, z', \theta)]. \tag{8}$$

This central-ray approximation for the attenuation factors saves computing time by more than 100-fold with less that 1% error (Liang *et al* 1989).

It can be shown (Liang *et al* 1994) that the attenuated convolution of (8) does not affect the depth–frequency relation (Lewitt *et al* 1989). Therefore, the depth-dependent convolution can be deconvolved. The depth-dependent deconvolution for the resolution-restored projection $p(\xi, z, \theta)$ is expressed, in frequency space, as (Glick *et al* 1994, Ye and Liang 1994a, b)

$$P(\omega_\xi, \omega_z, \omega_\theta) = H^{-1}(\omega_\xi, \omega_z, \mathrm{RoR} - \omega_\theta/\omega_\xi)\tilde{P}_p(\omega_\xi, \omega_z, \omega_\theta) \tag{9}$$

where $\tilde{P}_p$ and P are the three-dimensional (3D) Fourier transform (FT) of $p_p(\xi, z, \theta)$ and $p(\xi, z, \theta)$, respectively, with ω_ξ being the spatial frequency along the ξ axis, ω_z the spatial frequency along the z axis and ω_θ the angular frequency of θ. The inverse $H^{-1}(\omega_\xi, \omega_z, \eta) = 1/H(\omega_\xi, \omega_z, \eta)$, and $H(\omega_\xi, \omega_z, \eta)$ is the 2D FT of the detector-response kernel $h(\xi, z, \eta)$ at a depth indicated by η. In order to avoid $H^{-1} \to \infty$ when $H \to 0$, a modification is made such that $H^{-1} = 1/(H + \zeta)$, where ζ is a small constant (=0.01).

(4) *Compensation for body attenuation.* After the depth-dependent deconvolution (via an inverse FT), we obtain the attenuated line integral (or attenuated Radon transform) $p(\xi, z, \theta)$ (Gullberg 1979). Now the 3D reconstruction of the attenuated line integrals becomes a 2D problem (for parallel-beam geometry), since the volume reconstruction can be performed slice by slice along the z axis. For cone-beam geometry, the reconstruction is performed in three dimensions. In this work, we will focus on parallel-beam geometry, i.e.

$$p(\xi, \theta) = \int_{-\infty}^{\infty} \mathrm{d}\eta \, o(x, y) \exp\left[- \int_{-\infty}^{\eta} \mu(x', y') \, \mathrm{d}\eta' \right] \tag{10}$$

where the integral for the attenuation factor starts from bin (ξ, θ) along ray i (parallel to the η axis, see figure 1) until the source point $o(x, y)$ in the stationary coordinates.

In some special cases, for example when radiotracer distributes only within the area of heart (or breasts) and does not go into the lungs and other soft tissues off away from the heart (or breasts), the attenuated Radon transform can be accurately inverted for solution $o(x, y)$ (Glick *et al* 1995, Liang *et al* 1994). Under this special condition, the analytical inversion is the choice for the attenuation compensation and the image reconstruction. However, for general cases in which the lungs are the target (Alavi 1977) or the heart (or breasts) is the target but the radiotracer in the lungs and soft tissues away from the heart (or breasts) is not negligible, the analytical inversion is mathematically impractical. A fast-convergent iterative technique is then an alternative choice for the solution $o(x, y)$ of (10).

Given the attenuation map $\mu(x, y)$ for each slice, the source in that slice can be reconstructed by an iterative FBP (IFBP) algorithm (Liang 1991), although other fast-convergent algorithms could be employed (Bouman and Sauer 1996, Clinthorne *et al* 1993, Hudson and Larkin 1994)

$$o_k^{(n+1)} = \bar{o}_k^{(n)} + \mathrm{FBP}[p - p^{(n)}]_k / f_k(\mu) \tag{11}$$

where $p^{(n)}$ is the projected data from the nth iterated estimate $o^{(n)}$ by (10), FBP$[p - p^{(n)}]$ represents the FBP reconstruction of the data difference $(p - p^{(n)})$ (Huesman *et al* 1977), $f(\mu)$ stands for the attenuation weighting factors and $\bar{o}$ is an average over nearby pixels.

Equation (11) is the mathematical formula for the attenuation compensation and image reconstruction, after noise treatment, scatter subtraction and resolution deconvolution. Implementation of these four steps is delineated below.

4. Implementation

The implementation of the reconstruction method on a digital computer consists of the following two steps: (1) data acquisition and (2) image reconstruction.

(1) *Data acquisition.* Three sets of data are required to reconstruct the quantitative image: (a) the point source measurements for the detector-response kernel, (b) the transmission scans for the attenuation map and (c) the multiple-energy-window emission data.

(a) *Point source measurements.* A point-source measurement is necessary to construct the detector-resolution kernel for the depth-dependent deconvolution of (9). For ^{99m}Tc radiotracer, as used in this study, a point source of 3.7×10^7 Bq (or 1 mCi) activity and 1.5 mm in radius was used. The measurement was performed by positioning the point source in air at depths of 1, 5, 10, 15, 20, 25, 30, 35, 40 and 45 cm, respectively, from the collimator surface. A low-energy, high-resolution, parallel-hole collimator was employed with a GE SPECT system. The photopeak-energy window was centred at 140 keV with 20% width. The acquired image array at each depth was 128^2 with an FOV of 45^2 cm^2, i.e., the pixel size was 3.5 mm. The counts of each image were 10 000. The kernel at 128 depths (at 3.5 mm increment from collimator surface) was constructed by interpolation of the measured images via cubic fitting, so the kernel was an array of 128^3 size. Since the detector-response kernel is system specific, it is determined only once for the chosen radiotracer and collimator/detector system. The kernel was then stored in the computer for all later applications.

(b) *Transmission scans.* Transmission scans are necessary for an object-specific attenuation map of each patient (Bailey *et al* 1987, Hasegawa *et al* 1990, Liang and Ye 1994), although some *ad hoc* approaches based on segmentation techniques and emission data have been proposed (Pan *et al* 1996). A flood source of 1.11×10^9 Bq (or 30 mCi) ^{99m}Tc activity and size of the same as the FOV (i.e., 45^2 cm^2) was used. A chest phantom (Data Spectrum, NC) filled with water was placed on the patient bed with marks on both the phantom and bed for later repeating measurements. The chest phantom consists of three parts: (a) a cylindrical elliptical tank made of Plexiglass; (b) lung inserts made of styrofoam beads alone which has a density close to that of the air and (c) a spine insert consisting of packed bone meal. A cross section of the phantom is depicted on the top left of figure 3 (without the cardiac insert). The cylindrical elliptical tank has a major axis of 32 cm, minor axis of 23 cm and height of 21 cm. The lung inserts are cut to the shape with somewhat variation along the z axis. The spinal insert is a cylinder of 3 cm diameter. This phantom mimics a part of the torso for a person at weight around 70 kg (Tsui *et al* 1989). A circular orbit of scans was employed with 128 evenly spaced stops. The energy window was set at the centre of 140 keV with 20% width (the same as the point-source measurements). At each stop, an acquisition of 10 seconds was taken. The total counts were approximately 28.5 million. The data were reconstructed by a FBP method with a low-pass Butterworth window on the Ramp filter at 0.5 Nyquist frequency cutoff and a power factor of 5 (Huesman *et al* 1977). Since the phantom occupied less than half of 128 slices, only the central 64 slices were reconstructed. A slice of the 3D reconstructed object-specific attenuation map is shown on the bottom left of figure 3.

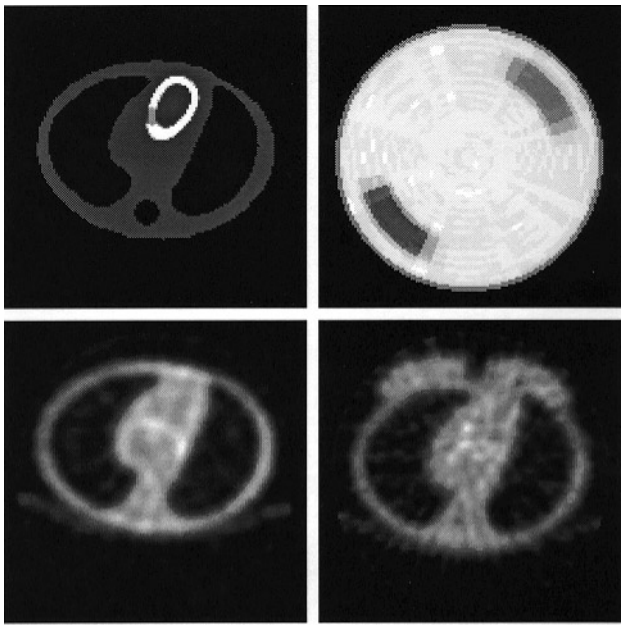

Figure 3. A slice of a 3D chest emission phantom (top left), the bullseye display of the 3D myocardial activity in the emission phantom (top right), a slice of a 3D attenuation map of a male chest model reconstructed from transmission scans (bottom left) and a slice of a 3D female chest model attenuation map obtained from transmission data (bottom right).

(c) *Emission data acquisition.* Emission data were acquired using the same SPECT system after the phantom was filled in with radiotracer solutions as specified below. The chest phantom was modified by including a cardiac insert and related support assembly made of Plexiglass (see the top left of figure 3). The cardiac insert simulates the left ventricle of the heart. The insert consists of two concentric cylinders with a half-spherical end cap on each end. The inner cylinder forms the ventricular chamber with 8 cm length and 4 cm diameter. The space between the two cylinders forms the myocardial wall chamber of 1 cm thickness. Tracer solution with different concentration can fill in the chambers separately. In the experiment, the myocardial wall chamber was filled with 2.78×10^5 Bq cm^{-3} (or 7.5 mCi cm^{-3}) ^{99m}Tc sestamibi solution, which is referred to as 100% perfusion concentration later on. Two defect inserts were placed inside the myocardial wall chamber at anterolateral and inferoseptal positions, respectively. The one in the inferoseptal wall (defect 1) had 25% concentration and the other one in the anterolateral wall (defect 2) had 50% concentration. The defect shown in the cross section of the heart is defect 1. On the bullseye display (top right of figure 3), defect 1 is on the bottom left and defect 2 on the top right. These two defects have the same size of angular span of 45 degrees in the wall of the myocardial chamber. The thickness is of 1 cm and length of 2 cm. The space inside the inner cylinder (or the ventricular chamber) and the 'soft-tissue' region across the FOV had a tracer solution of 5%. The 'lungs' and 'spinal bone', as well as the outside regions (i.e., the cylindrical tank walls) had no activity. The above tracer distribution represents a typical extraction fraction of clinical myocardial perfusion studies using ^{99m}Tc sestamibi (Garcia *et al* 1990). The emission scans had 128 stops evenly spaced on a circle of 20 cm radius. Each scan matrix had a sample size of 128^2. The photopeak-energy window settings

remained the same (i.e., from 126 to 154 keV). The off-photopeak or scatter-energy window ranged from 90 to 126 keV. The scanning time was 14 seconds at each stop. The total counts were approximately 7.1 million from the photopeak-energy window and 4.3 million from the scatter-energy window. Only the central 64 slices of emission data were used for reconstructions, since the samples off the central 64 slices were zero.

(2) *Image reconstruction.* Reconstruction of the acquired emission data for the tracer-uptake image requires compensation for all the statistical and physical degradation effects associated with the photon emission, transport and detection. The major ones are described below.

(a) *Smoothing of Poisson noise.* The Poisson noise embedded in both the photopeak and scatter-window samples was treated first by the square-root transformation (Anscombe 1948). The mean of each transformed datum was then estimated by a Wiener filtering approach (Chang *et al* 1996). In the filtering, a collimator-specific treatment for the dual samplings of collimator holes and photomultiplier tubes was performed (Li *et al* 1997). The estimated means were then square-transformed back to the projection space. These modified projection data are the estimate of the means of the photopeak (i.e., $\tilde{p}_p$, see (2)) and scatter-window (i.e., p_s) data. It is noted that the estimated means of the scatter-window data are not p_s, since the scatter-window measurement contains both the primary and scattered photons.

(b) *Correction for isotope decay.* Following the smoothing of Poisson noise, a correction for the isotope decay was applied to the modified photopeak and scatter-window projection data, given the half life (or decay rate λ) of the isotope and the acquisition time τ per view. The correction factor is $\exp(\mathrm{i}\lambda\tau)$, where $i = 0, 1, 2, \ldots$, is the projection index; $i = 0$ means the first view.

(c) *Subtraction of scattered photons.* The estimated scatter contributions p_s by (7) were subtracted from the photopeak data $\tilde{p}_p$ bin by bin in the projection space. This subtraction approximately removes the tails of the photopeak-window projection profiles of a small object in attenuating media (Liang 1991). An underlying assumption is made for the scatter subtraction that the tails are the consequence of the scatter (Liang *et al* 1989). The subtraction also minimizes the background contribution to the photopeak data.

(d) *Recovery of detector resolution.* After the scatter subtraction, the primary-photon contribution p_p to the photopeak-window measurement is deconvolved by (9). A fast FT (FFT) program was applied to the 3D sinogram of $p_p(\xi, z, \theta)$ for $P_p(\omega_\xi, \omega_z, \omega_\theta)$ and to the 2D resolution kernel $h(\xi, z, \eta)$ at each depth $\mathrm{RoR} + \eta$ for $H(\omega_\xi, \omega_z, \eta)$. The values of $P_p(\omega_\xi, \omega_z, \omega_\theta)$ were multiplied by $H^{-1}(\omega_\xi, \omega_z, \mathrm{RoR} - \omega_\theta/\omega_\xi)$ in the frequency space for $P(\omega_\xi, \omega_z, \omega_\theta)$. After the multiplication, an inverse 3D FFT generated $p(\xi, z, \theta)$, see (10).

(e) *Image reconstruction via iterative FBP.* At the beginning, the attenuation weighting factors $\{f_k\}$ were computed for each slice. This was done by backprojecting a unit projection through the attenuation map (the same implementation in EM-type reconstruction (Fessler 1995, Liang and Hart 1988)). A 2D FBP reconstruction of the line integral $p(\xi, \theta)$ at each slice was performed with a low-pass Hann window on the Ramp filter at the Nyquist frequency cutoff (Huesman *et al* 1977). This FBP reconstruction is widely referred to as conventional FBP procedure. The initial estimate (or zeroth iteration) of the source was then obtained from the FBP reconstruction divided by the attenuation weighting factors. This initial estimation is similar to Chang's (1978) multiplicative attenuation correction, but in a different (accurate) way in computing the attenuation weighting factors.

From the nth iterated estimate, a projection operator generated $p^{(n)}$ via (10). By the FBP reconstruction on the difference $p - p^{(n)}$ with the Hann filter and the division by $f(\mu)$

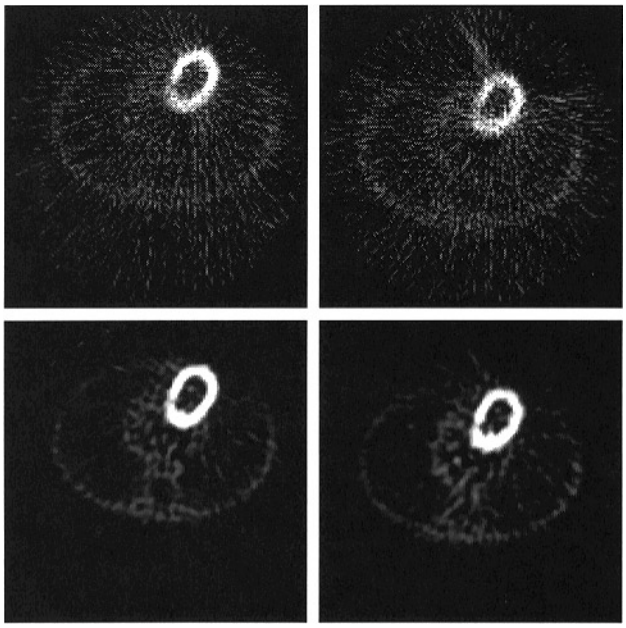

Figure 4. A slice of 3D reconstructed images of the emission phantom by the conventional FBP method (top left is from the male model and top right from the female model) and by the quantitative approach (bottom left is from the male model and bottom right from the female model).

pixel by pixel, we had the update term of (11). By adding the update term to the smoothed nth iterated estimate (over nearby pixels (Liang 1991)), we obtained the $(n+1)$th iterated source distribution. The iteration converged to a nearly stable solution after two iterations. This iterative procedure is the same as those additive update algorithms (Bouman and Sauer 1996, Chang 1978, Clinthorne *et al* 1993, Wallis and Miller 1993, Xu *et al* 1993). However, the local smoothing over nearby pixels preserves edge details and prevents iterations from divergence.

In computing the attenuation weighting factors $\{f_k\}$ and projecting the estimated source $\{o_k^{(n)}\}$ to $\{p_i^{(n)}\}$, the Siddon method was coded to recursively trace these values along each projection ray. This method is accurate and efficient in calculating the intersecting lengths of rays within pixels, given the starting and ending points of each path.

5. Results

We validated the efficient quantitative approach by the following means: (a) compare the quantitative accuracy between the reconstructions of the simultaneous compensation approach and the conventional FBP method and (b) study the performance of the approach for different body characteristics, such as the thorax of male and female models. Two experiments were performed.

In the first experiment, we used an attenuating thorax phantom of the male model. The attenuation map of FBP reconstruction from transmission scans is shown on the bottom left of figure 3. The emission phantom is depicted on the top left of that figure. On the top right is the bullseye display of the myocardial activity. Quantitative analysis on the

bullseye representation is widely used for myocardial perfusion SPECT study. Three regions of interests (ROIs) were selected on the bullseye display. The first ROI was selected for defect 1 (25% concentration) on the bottom left of the bullseye display. The second one was chosen for defect 2 (50% concentration) on the top right. The whole myocardium, except for the two defects, was selected for the third ROI. The ROIs for the defects have the same size of 500 pixels. The third ROI contains 8700 pixels. In the second experiment, the thorax phantom was modified by adding two breasts (water bags) to simulate a female model. The water bag, when attached to the phantom on the top (see figure 3), is a rounded disc of 8 cm diameter and 4 cm thick. The FBP reconstructed attenuation map from transmission scans of the second phantom is shown on the bottom right of figure 3. The emission configuration remained the same, as shown on the top left of that figure.

A slice of 3D reconstructed images of $128^2 \times 64$ size is shown by figure 4. On the top are the conventional FBP reconstructions (a low-pass Hann window on the Ramp filter at the Nyquist frequency cutoff) and on the bottom are the quantitative approach results. The images on the left are reconstructions of the male model and on the right are the results of the female model. This figure shows qualitatively the performance of the reconstruction techniques. By visual inspection, it can be concluded that the conventional FBP reconstruction varies for different body models (top row). The quality in the target areas of myocardium, lungs and soft tissues near the heart are poor, as compared to that of the quantitative reconstructions (bottom row). The quantitative reconstructions are similar, as expected, for the two different body models.

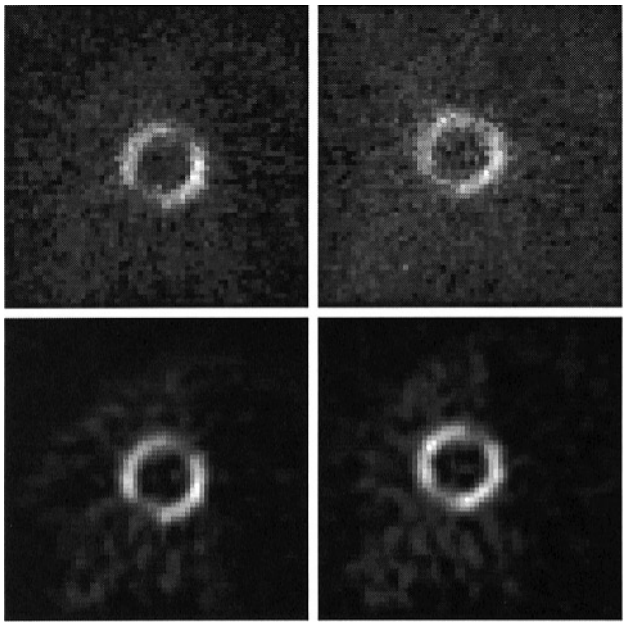

Figure 5. A slice through the short axes of the heart in the reconstructed 3D emission images of figure 4. The slice contains the two defects. On the top are the conventional FBP reconstructions (left is from the male model and right from the female model). The results of the quantitative approach are shown on the bottom (left is from the male model and right from the female model).

In order to see more details on the heart, we extracted a cross section containing the two defects through the short axes of the heart. The slice images are shown by figure 5.

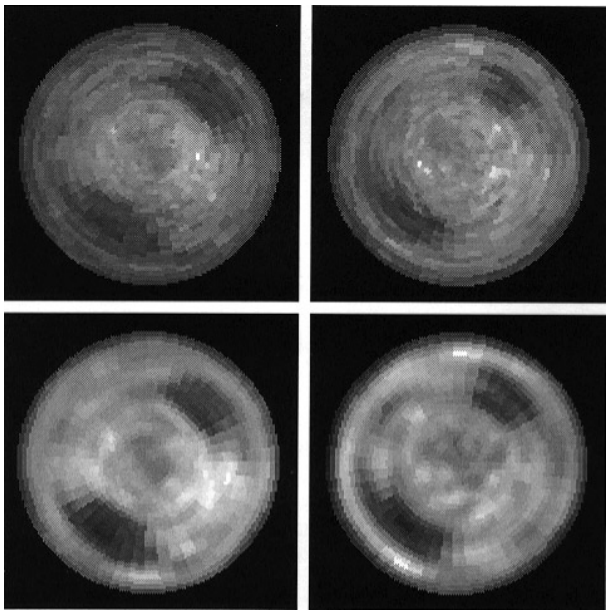

Figure 6. The bullseye display of the myocardial activity of the reconstructed 3D emission images in figure 4. On the top are the conventional FBP reconstructions (left is from the male model and right from the female model). On the bottom are the results of the quantitative approach (left is from the male model and right from the female model).

The defect on the top right is defect 2. Defect 1 is on the bottom left. The variation on different body models is clearly seen from the top images of the conventional FBP method (the left one is from the male model and right one from the female model). The similarity and improved quality of the reconstructions by the efficient quantitative approach are clearly noticed. Cardiac short-axis images of the left ventricle are the most clinically relevant for the majority of diagnostic imaging purposes.

The bullseye display of the myocardial activity from the 3D reconstructions of figure 4 is shown by figure 6. The variation and lower quality of the conventional FBP reconstruction are again observed. The quality improvement by the quantitative approach is significant. The consistent performance of the quantitative approach for different body characteristics is again clearly seen. Quantitative ROI measures on the bullseye displays of figure 6 are documented by table 1.

Table 1. Intensity means and deviations for the ROIs on the bullseye display.

		μ_1	σ_1	μ_2	σ_2	μ_3	σ_3
FBP							
	true	2.50	0.00	5.00	0.00	10.00	0.00
	no_breasts	1.59	0.21	2.05	0.23	3.00	0.34
	with_breasts	1.42	0.13	1.81	0.18	2.31	0.22
IFBP							
	no_breasts	3.47	0.75	4.86	0.94	8.18	0.76
	with_breasts	3.51	0.76	4.85	0.91	8.23	0.73

The ROI means and standard deviations (μ_1, σ_1) were computed from defect 1 (25% concentration), (μ_2, σ_2) from defect 2 (50% concentration) and (μ_3, σ_3) from the normal myocardium of the third ROI (100% concentration). The variation of μ_1 with_breasts from the phantom value is $|1.42 - 2.50|/2.50 = 43\%$ for FBP and 40% for IFBP; for μ_2 the variation is 64% for FBP and 3% for IFBP and for μ_3 the variation is 77% for FBP and 18% for IFBP. The variation of μ_1 from no_breasts to with_breasts is $|1.59 - 1.42|/1.59 = 11\%$ for FBP and 1% for IFBP; for σ_1 the variation is 38% for FBP and 1% for IFBP; for μ_2 the variation is 12% for FBP and less than 1% for IFBP; for σ_2 the variation is 22% for FBP and 3% for IFBP; for μ_3 the variation is 23% for FBP and less than 1% for IFBP and for σ_3 the variation is 35% for FBP and 4% for IFBP. The quantitative improvement and consistent performance of the efficient simultaneous compensation approach (or IFBP) for the heart are demonstrated by these experimental phantom studies.

The reconstruction of the lung regions shows significant improvement with the quantitative approach, as compared to the conventional FBP method, see figure 4. It is difficult to draw ROIs on the lungs of the conventional FBP reconstructions. So we selected two regions each on the left and right lungs of the quantitative reconstructions. The region contains 450 pixels for each slice. Three slices were chosen, one above and one below the slice of figure 4. The means and standard deviations are listed in table 2. The quantitative improvement and consistent performance of the efficient simultaneous compensation approach are clearly seen for the lungs as well.

Table 2. Intensity means and deviations of ROIs for the lungs.

	True		FBP		IFBP	
	μ	σ	μ	σ	μ	σ
no_breasts	0.0	0.0	0.14	0.17	0.10	0.15
with_breasts	0.0	0.0	0.13	0.16	0.11	0.16

For the soft tissues around the heart, an ROI was drawn with 400 pixels on each slice and a total of three slices were chosen around the slice of figure 4. The ROI means and standard deviations are given by table 3.

Table 3. Intensity means and deviations of ROI for the soft tissues near the heart.

	True		FBP		IFBP	
	μ	σ	μ	σ	μ	σ
no_breasts	0.5	0.0	0.24	0.25	0.51	0.37
with_breasts	0.5	0.0	0.20	0.11	0.60	0.43

It is easy to see the quantitative improvement and consistent performance of the compensated reconstruction.

It is noted that the above results reflect only the relative quantification between phantom experiments and patient studies, although the quantitative reconstruction demonstrated its necessity for clinical use. A few factors can deviate the quantitative measurements due to the artificially constructed phantoms, such as the phantom shape and size, the lung material and the bone configuration.

The reconstruction time of a $128^2 \times 64$ image array from 128 projections of 128×64 size by the conventional FBP was less than one minute on an HP/730 desktop computer. The reconstruction by the quantitative approach finished in less than 15 minutes. The programs were coded in C language. Further reduction of computing time can be achieved by optimizing the programs.

6. Discussion

Although mathematically exact implementations of (1)–(5) are possible based on Bayesian inference and iterative efficient numerical techniques, they are not practical in clinical applications due to the heavy computing burden (Bouman and Sauer 1996, Clinthorne *et al* 1993, Xu *et al* 1993). On the other hand, analytical approaches to the inverse problem have a great computing advantage, but they may not be applicable for general cases in chest imaging (Gullberg 1979, Liang *et al* 1989). For brain and some special chest imaging cases (such as breast and heart SPECT imaging with negligible activity in the lungs and soft tissues away from the myocardium or breasts), the analytical approach is the choice (Glick *et al* 1995, Liang *et al* 1994). For general SPECT studies on the heart and lungs, efficient simultaneous compensation approaches with the computing potential of analytical inversion are demanded. The techniques developed by this work aim toward that goal.

Since heart disease has the highest prevalence across this nation, cost-effective diagnostic means are very necessary. Quantitative cardiac SPECT is a cost-effective diagnostic modality. Development and implementation of quantitative cardiac SPECT protocols have been a research topic for many years. The objective of this research is to develop the cost-effective approach to heart diagnoses, as well as lung and breast studies. The clinical value of this efficient quantitative approach is significant, in terms of reconstruction accuracy and computational efficiency. Further investigation on the simultaneous approach, optimization of the implementation and clinical validation of the approach on more realistic phantoms and patient data are under consideration. It is noted that because of the relatively small size of the phantom and the fact that the lungs were made of Styrofoam, having essentially the density of air and containing no activity, further research is required to determine whether these results are valid for other more realistic source geometries.

Acknowledgments

This work was supported by grant No HL51466, awarded by the National Heart, Lung, and Blood Institute; grant No NS33853, awarded by the National Institute of Neurological Disorders and Stroke; and an Established Investigator Award from the American Heart Association.

References

Alavi A 1977 Perfusion-ventilation lung scans in the diagnosis of pulmonary thromboembolism *Appl. Radiology* **6** 182–8

Anscombe F 1948 The transformation of Poisson, binomial and negative-binomial data *Biometrika* **35** 246–54

Bailey D, Hutton B and Walker P 1987 Improved SPECT using simultaneous emission and transmission tomography *J. Nucl. Med.* **28** 844–51

Bartlett M, Bacharach S, Voipio-Pulkki L and Dilsizian V 1995 Artifactual inhomogeneities in myocardial PET and SPECT scans in normal subjects *J. Nucl. Med.* **36** 188–95

Berman D S, Kiat H, Van Train K, Garcia E, Friedman J and Maddahi J 1991 Tc-99m sestamibi in the assessment of chronic CAD *Semin. Nucl. Med.* **21** 190–212

Bouman C and Sauer K A 1996 Unified approach to statistical tomography using coordinate descent optimization *IEEE Trans. Image Process.* **5** 480–92

Chang L A 1978 Method for attenuation correction in radionuclide CT *IEEE Trans. Nucl. Sci.* **25** 638–43

Cheng J, Liang Z, Ye J, Cabahug C, Oster Z and Harrington D 1996 Accurate treatment of Poisson noise for quantitative reconstruction of brain SPECT *J. Nucl. Med.* **37** 218

Clinthorne N, Pan T, Chiao P, Rogers W and Stamos J 1993 Preconditioning methods for improved convergence rates in iterative reconstructions *IEEE Trans. Med. Imaging* **12** 78–83

DePuey E and Garcia E 1989 Optimal specificity of Tl-201 SPECT through recognition of imaging artifacts *J. Nucl. Med.* **30** 441–9

Eisner R L, Schmarkey L S, Martin S E, Carey D, Worthy M A, Chu T H, Horowitz S F and Patterson R E 1994 Defects on SPECT 'perfusion' images can occur due to abnormal segmental contraction *J. Nucl. Med.* **35** 638–43

Fessler J 1995 Penalized ML image reconstruction using space-alternating generalized EM algorithms *IEEE Trans. Image Process.* **4** 1417–25

Floyd C, Jaszczak R, Greer K and Coleman E 1986 Inverse Monte Carlo as a unified reconstruction algorithm for ECT *J. Nucl. Med.* **27** 1577–85

Furuie S and Mascarenhas N 1992 Tomographic Reconstruction of images with Poisson noise: projection estimation *Automedica* **15** 133–40

Galt J, Garcia E and Robbins W 1990 Effects of myocardial wall thickness on SPECT quantification *IEEE Trans. Med. Imaging* **9** 144–50

Garcia E V *et al* 1990 Technical aspects of myocardial SPECT imaging with Tc-99m sestamibi *Am. J. Cardiol.* **66** 23E–31E

Glick S, King M, Pan T and Soares E 1995 An analytical approach for compensation of nonuniform attenuation in cardiac SPECT imaging *Phys. Med. Biol.* **40** 1677–93

Glick S, Penney B, King M and Byrne C 1994 Noniterative compensation of photon attenuation and the distance-dependent detector response in SPECT imaging *IEEE Trans. Med. Imaging* **13** 363–74

Gullberg G 1979 The attenuated radon transform: theory and application in medicine and biology *PhD Thesis* Donner Laboratory, University of California

Hasegawa B, Gingold E, Reilly S, Liew S and Cann C 1990 Description of a simultaneous emission–transmission CT system *Proc. SPIE* **1231** 50–60

Hudson H and Larkin R 1994 Accelerated image reconstruction using ordered subsets of projection data *IEEE Trans. Med. Imaging* **13** 601–9

Huesman R, Gullberg G, Greenberg W and Budinger T 1977 *Donner Algorithms for Reconstruction Tomography* (Berkeley, CA: University of California)

Jaszczak R, Greer K, Floyd C, Harris C and Coleman E 1984 Improved SPECT quantification using compensation for scattered photons *J. Nucl. Med.* **25** 893–900

King M, Doherty P and Schwinger R 1983 A Wiener filter for NM images *Med. Phys.* **10** 876–80

King M, Hademenos G and Glick S A 1992 Dual-photopeak window method for scatter correction *J. Nucl. Med.* **33** 605–12

Lewitt R, Edholm P and Xia W 1989 Fourier method for correction of depth-dependent collimator blurring *Proc. SPIE* **1092** 232–43

Li J, Liang Z, Kuan H, Wong C, Cheng J, Wang G, Schlyer D, Volkow N and Harrington D 1997 A collimator-specific treatment of data for F-18 SPECT imaging *J. Nucl. Med.* **38** 211

Liang Z 1991 Compensation for nonuniform attenuation, scattering, and collimator response with an iterative FBP method for SPECT reconstruction *Radiology* **181** 186

Liang Z and Hart H 1988 Bayesian reconstruction in emission computerized tomography *IEEE Trans. Nucl. Sci.* **35** 877–85

Liang Z, Jaszczak R, Floyd C, Greer K and Coleman E 1989 Reprojection and backprojection in SPECT image reconstruction *Proc. IEEE, Energ. Inform. Tech. Southeast (Columbia, SC, 1989)* vol 2, pp 919–26

Liang Z and Ye J 1994 Reconstruction of object-specific attenuation map for quantitative SPECT *Conf. Record IEEE Nuclear Science Symp.–Medical Imaging Conf. (San Francisco, CA, 1993)* vol 2, pp 1231–5

Liang Z, Ye J and Harrington D 1994 Analytical approach to quantitative brain SPECT with nonuniform attenuation *Med. Phys.* **21** 915

Links J, Jeremy R, Dyer S, Frank T and Becker L 1990 Wiener filtering improves quantification of regional myocardial perfusion with thallium-201 SPECT *J. Nucl. Med.* **31** 1230–6

Maurea S, Cuocolo A, Soricelli A, Castelli L, Squame F, Imbriaco M, De Luca N, Trimarco B and Salvatore M 1995 Myocardial viability index in CAD: Tc-99m methoxy isobutyl isonitrile redistribution *J. Nucl. Med.* **36** 1953–60

Moore S, Kijewski M, Mueller S and Holman B 1988 SPECT image noise power: effects of nonstationary projection noise and attenuation compensation *J. Nucl. Med.* **29** 1704–9

Nakajima K, Taki J, Shuke N, Bunko H, Takata S and Hisada 1993 Myocardial perfusion imaging and dynamic analysis with Tc-99m tetrofosmin *J. Nucl. Med.* **34** 1478–84

Ogawa K, Harata Y, Ichihara T, Kubo A and Hashimoto S 1991 A practical method for position-dependent Compton-scatter correction in SPECT *IEEE Trans. Med. Imaging* **10** 408–12

Pan T, King M, deVries D and Ljungberg M 1996 Segmentation of the body and lungs from Compton scatter and photopeak window data in SPECT: a Monte Carlo investigation *IEEE Trans. Med. Imaging* **15** 13–24

Tsui B and Gullberg G 1990 The geometric transfer function for cone and fan beam collimators *Phys. Med. Biol.* **35** 81–93

Tsui B, Gullberg G, Edgerton E, Ballard J, Perry J, McCartney W and Berg J 1989 Correction of nonuniform attenuation in cardiac SPECT imaging *J. Nucl. Med.* **30** 497–507

Van Train K F *et al* 1980 Quantitative same-day rest-stress Tc-99m sestamibi SPECT: definition and validation of stress normal limits and criteria for abnormality *J. Nucl. Med.* **34** 1494–1502

Wallis J and Miller T 1993 Rapidly converging iterative reconstruction algorithms in SPECT *J. Nucl. Med.* **34** 1793–1800

Xu L, Liow J and Strother S 1993 Iterative algebraic reconstruction algorithms for ECT: a unified framework and its application to PET *Med. Phys.* **20** 1675–84

Ye J and Liang Z 1994a Depth-dependent resolution deconvolution for myocardial perfusion SPECT with noncircular scan orbit *J. Nucl. Med.* **35** 190

——1994b Comparison of 180° and 360° myocardial perfusion SPECT with nonuniform attenuation compensation and depth-dependent resolution deconvolution *Med. Phys.* **21** 916

Zeng G and Gullberg G 1991 3D iterative reconstruction algorithms with attenuation and geometric point response correction *IEEE Trans. Nucl. Sci.* **38** 693–702